

Enhancing spiral microrobot dynamics in ratchet potentials: The role of Gaussian colored noise

Xinpeng Shi(史鑫鹏) and Kheder Suleiman
Citation: Chin. Phys. B, 2026, 35 (**4**): 040203. DOI: 10.1088/1674-1056/ae0c00
http://cpb.iphy.ac.cn; http://iopscience.iop.org/cpb

What follows is a list of articles you may be interested in

Study and application of solitary wave propagation at fractional order of time based on SPH method

Luyang Ma(马璐阳), Rahmatjan Imin(热合买提江·依明), and Azhar Halik(艾孜海尔·哈力克)
Chin. Phys. B, 2025, 34 (**5**): 050202. DOI: 10.1088/1674-1056/adbd2a

Molecular dynamics study of interactions between edge dislocation and irradiation-induced defects in Fe–10Ni–20Cr alloy

Tao-Wen Xiong(熊涛文), Xiao-Ping Chen(陈小平), Ye-Ping Lin(林也平), Xin-Fu He(贺新福), Wen Yang(杨文), Wang-Yu Hu(胡望宇), Fei Gao(高飞), and Hui-Qiu Deng(邓辉球)
Chin. Phys. B, 2023, 32 (**2**): 020206. DOI: 10.1088/1674-1056/ac7dba

Self-adaptive behavior of nunchakus-like tracer induced by active Brownian particles

Yi-Qi Xia(夏益祺), Guo-Qiang Feng(冯国强), and Zhuang-Lin Shen(谌庄琳)
Chin. Phys. B, 2022, 31 (**4**): 040204. DOI: 10.1088/1674-1056/ac29b1

Magnetization relaxation of uniaxial anisotropic ferromagnetic particles with linear reaction dynamics driven by DC/AC magnetic field

Yu-Song Hu(胡玉松), Min Jiang(江敏), Tao Hong(洪涛), Zheng-Ming Tang(唐正明), and Ka-Ma Huang(黄卡玛)
Chin. Phys. B, 2021, 30 (**9**): 090202. DOI: 10.1088/1674-1056/abeb0b

Atomistic simulations of the lubricative mechanism of a nano-alkane lubricating film between two layers of Cu-Zn alloy

Jing Li(李京), Peng Zhu(朱鹏), Yuan-Yuan Sheng(盛圆圆), Lin Liu(刘麟), and Yong Luo(罗勇)
Chin. Phys. B, 2021, 30 (**8**): 080205. DOI: 10.1088/1674-1056/abfbd6

Enhancing spiral microrobot dynamics in ratchet potentials: The role of Gaussian colored noise

Xinpeng Shi(史鑫鹏) and Kheder Suleiman†

School of Mathematics and Statistics, Northwestern Polytechnical University, Xi'an 710072, *China*

(Received 12 August 2025; revised manuscript received 22 September 2025; accepted manuscript online 26 September 2025)

Random disturbances in microfluidic environments often cause pronounced trajectory deviations in microrobots, posing challenges for robust control. However, most existing models either neglect these disturbances or idealize them as Gaussian white noise, limiting their applicability. To address this, we investigate the influence of Gaussian colored noise (GCN) on the dynamics of a spiral microrobot navigating a ratchet potential. A stochastic dynamic model grounded in resistive force theory is proposed, and the system's response is analyzed using the steady-state probability density function. We systematically examine how variations in ratchet potential, fluid viscosity, and noise intensity affect the microrobot's average velocity and mean first passage time. Moreover, we explore how geometric design impacts propulsion efficiency under stochastic excitation. Results reveal that GCN can significantly enhance propulsion efficiency and promote directional transport, with these effects strongly dependent on the noise correlation time. These findings not only enrich the theoretical framework of noise-induced microrobot dynamics but also provide practical guidance for optimizing design and environmental parameters.

Keywords: spiral microrobot, Gaussian colored noise, ratchet potential, stochastic dynamic model

PACS: 02.70.Ns, 02.70.Uu, 02.50.Fz, 02.60.Cb

DOI: 10.1088/1674-1056/ae0c00 **CSTR:** 32038.14.CPB.ae0c00

1. Introduction

Microrobot technology has emerged as a transformative tool across fields such as biomedicine, environmental monitoring and precision manufacturing.[1–3] These miniature robots excel in performing intricate tasks within microenvironments, such as delivering chemotherapy drugs to tumor cells or performing minimally invasive retinal surgeries.[4–6] However, their precise control and motion prediction remain formidable challenges due to the complex interplay of scale effects, Brownian motion and fluid dynamics.[7–12] A comprehensive understanding of their motion mechanisms is thus critical for advancing both fundamental knowledge and practical applications.

Among microrobots, spiral microrobots have attracted considerable attention due to their unique motion mechanisms and high propulsion efficiency. Inspired by microorganisms such as bacteria, these microrobots navigate viscous fluids with remarkable effectiveness.[13–16] Their spiral tail design generates propulsion by rotating under external stimuli such as magnetic fields, enabling them to overcome viscous resistance and maneuver adeptly in microenvironments.[17–20] This propulsion mechanism offers significant advantages for biomedical applications, including enhanced precision and flexibility.

To address the control and stability challenges faced by spiral microrobots in viscous microenvironments, spatially asymmetric ratchet potentials have been widely adopted to create energy landscapes that guide and constrain their motion. These potentials introduce a directional bias, constraining microrobot motion to enhance stability and control.[21–25] Depending on the system design, such potentials can take various forms, including rocking and deterministic asymmetric profiles, and can be tailored by adjusting parameters such as amplitude, phase or spatial periodicity to meet specific control objectives.[26–30] They have proven instrumental in biomedical and microfluidic applications, including targeted drug delivery and precise navigation along complex trajectories.[31–33]

However, even with engineered control strategies such as ratchet potentials, the motion of microrobots remains highly susceptible to environmental fluctuations and noise. Therefore, accurately simulating their dynamics requires careful consideration of stochastic effects.[34–37] Idealized Gaussian white noise (GWN) fails to capture the temporal correlations inherent in complex system noise. In contrast, Gaussian colored noise (GCN), characterized by a non-zero correlation time, more accurately reflects the stochastic properties of real microenvironments, particularly in biological fluids.[38–40] GCN is often modeled using Ornstein–Uhlenbeck processes or related stochastic differential equations that incorporate memory effects, enabling the representation of time-correlated fluctuations more realistically than uncorrelated noise models. GCN has been widely applied in the study of active matter, microswimmer navigation and noise-induced transport phenomena.[41–45] Research shows that GCN influ-

†Corresponding author. E-mail: Suleiman.kheder@outlook.com

© 2026 Chinese Physical Society and IOP Publishing Ltd. All rights, including for text and data mining, AI training, and similar technologies, are reserved.

ences propulsion efficiency and motion patterns, with effects strongly dependent on its correlation time and intensity.[46,47] It has also been employed to investigate trajectory persistence, noise-induced drift and the dynamic stability of microrobots in confined or complex environments.[48–50] A thorough understanding of these dynamics is essential for improving microrobot design and functionality in real-world applications where fluctuating environmental conditions are significant.

This study examines the dynamics of a spiral microrobot navigating a spatially asymmetric ratchet potential under GCN, which more accurately reflects realistic noise characteristics. We develop a stochastic dynamic model based on resistive force theory and analyze the system's behavior through its steady-state probability density function. By systematically varying ratchet potential strength, fluid viscosity and noise intensity, we quantify their effects on the microrobot's average velocity, mean first passage time (MFPT) and propulsion efficiency. Additionally, we investigate how the microrobot's geometric design influences performance under stochastic excitation. Our findings demonstrate that GCN can significantly enhance propulsion efficiency and facilitate directional transport, with effects modulated by the noise correlation time. These insights advance the theoretical understanding of noise-induced microrobot dynamics and offer practical strategies for optimizing design and operational parameters in complex microfluidic environments.

This paper is structured as follows. Section 2 introduces the stochastic dynamic model describing the microrobot's behavior. In Section 3, the motion characteristics under GCN are analyzed and compared with those under GWN. The main conclusions are summarized in Section 4.

2. Model

This section analyzes a microrobot composed of a spherical load and a rigid helical tail, as shown in Fig. 1(a). The structural design is inspired by the locomotion mechanism of flagellated bacteria. In specific application scenarios, the spherical load serves as a payload module, enabling the microrobot to transport drugs, sensors or other miniature devices for precise targeted delivery or real-time monitoring. In contrast, the helical tail is responsible for generating propulsion, allowing the microrobot to move efficiently in fluid environments with a low Reynolds number. Its non-reciprocal motion enables it to overcome viscous resistance and achieve self-propulsion. This biomimetic configuration provides the microrobot with excellent maneuverability and controllability, supporting autonomous navigation through various complex environments.

In low Reynolds number regimes, inertial effects are typically negligible and conventional models often omit their influence on microrobot motion. However, to more accurately characterize the dynamic behavior of the microrobot across a broader range of practical applications, particularly in fluid media such as lipids and water, inertial effects are incorporated into the theoretical framework. The refinement enables detailed modeling of the microrobot's motion, capturing fundamental dynamic quantities such as velocity, acceleration and trajectory across both translation and rotation. The governing equations are listed below:[16]

$$\begin{aligned} m\ddot{X} &= -\dot{U}(X) + F_{\mathrm{t}} - F_{\mathrm{p}} + \xi_1(t), \\ J\ddot{\theta} &= T_{\mathrm{t}} - T_{\mathrm{p}} + \xi_2(t), \end{aligned} \tag{1}$$

where X represents the displacement along the forward direction, θ indicates the angular orientation and $U(X)$ is the ratchet potential. The forces F_{t} and F_{p} refer to the propulsion force induced by the tail and the resistive force caused by the load ball, respectively. The torques acting on the microrobot comprise the tail torque T_{t} and the resistive torque T_{p} due to the load ball in the X-direction. Taking into account that the microrobot is affected by noise $\xi_1(t)$ and $\xi_2(t)$.[51] We consider $\xi_1(t)$ to be induced by the ratchet potential or other microrobots, therefore assuming $\xi_1(t)$ to be an exponentially correlated GCN with zero mean and the correlation function $\langle \xi_1(t)\xi_1(t_0)\rangle = D_1 \exp(|t-t_0|/\tau_1)/\tau_1$ with correlation time $\tau_1 > 0$. $\xi_2(t)$ represents a zero mean GWN with the correlation function $\langle \xi_2(t)\xi_2(t_0)\rangle = 2D_2\delta(t-t_0)$, where D_i $(i=1,2)$ represents the noise intensity, $\langle\cdot\rangle$ denotes the expected value, and $\delta(\cdot)$ refers to the Dirac delta function.

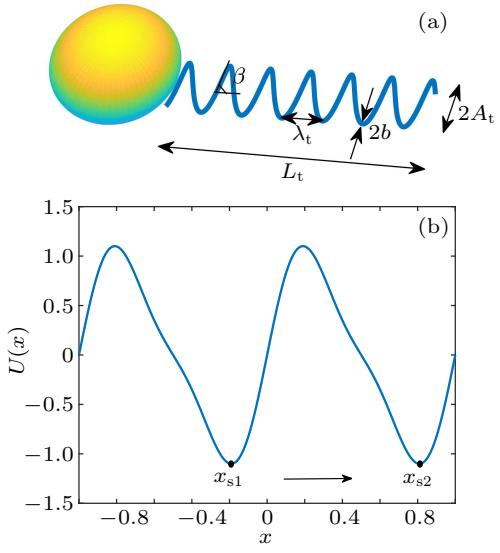


Fig. 1. Geometric structure of the spiral microrobot and ratchet potential field: (a) schematic of the spiral microrobot; (b) schematic of the applied ratchet potential.

The system's total mass and moment of inertia are defined as $m = m_{\mathrm{t}} + m_{\mathrm{p}}$ and $J = 2m_{\mathrm{p}}r^2/5 + m_{\mathrm{t}}b^2/2$, respectively. The load mass is calculated by $m_{\mathrm{p}} = 4\pi r^3\rho_{\mathrm{p}}/3$, and the tail mass by $m_{\mathrm{t}} = \pi b^2 L_{\mathrm{t}}\rho_{\mathrm{t}}$, where r, b and L_{t} denote the load radius, tail cross-sectional radius and tail length, respectively. ρ_{p} and ρ_{t} are the corresponding material densities.

By utilizing the interference and diffraction effects of the light field, an optical ratchet potential can be created. It is shown in Fig. 1(b), and the expression for the ratchet potential $U(X)$ with slope parameter U_0 and period L can be written as follows:

$$U(X) = U_0\left[\sin\left(\frac{2\pi X}{L}\right) + 0.25\sin\left(\frac{4\pi X}{L}\right)\right]. \tag{2}$$

The force and torque generated by the tail have the forms[52]

$$\begin{aligned} F_{\rm t} &= -L_{\rm t}(C_{\rm tn}\sin^2\beta + C_{\rm tt}\cos^2\beta)\sec\beta\dot{X} \\ &\quad + L_{\rm t}(C_{\rm tt} - C_{\rm tn})A_{\rm t}\sin\beta\dot{\theta}, \\ T_{\rm t} &= M_{\rm vt} + M_{\rm dt}, \end{aligned} \tag{3}$$

where the viscous torque $M_{\rm vt} = 4\pi\mu b^2 L_{\rm t}\cos\beta\dot{\theta}$ and the driving torque $M_{\rm dt} = L_{\rm t}(C_{\rm tt} - C_{\rm tn})A_{\rm t}\sin\beta\dot{X} + L_{\rm t}(C_{\rm tt}\sin^2\beta + C_{\rm tn}\cos^2\beta)A_{\rm t}^2\sec\beta\dot{\theta}$. $A_{\rm t}$ refers to the tail amplitude and μ refers to the fluid viscosity. The tail's pitch angle β is determined by the relation $\beta = \arctan(2\pi A_{\rm t}/\lambda_{\rm t})$ and $\lambda_{\rm t}$ is the tail wavelength. $C_{\rm tt} = 2\pi\mu/[\ln(2\lambda_{\rm t}/b) - 1/2]$ and $C_{\rm tn} = 4\pi\mu/[\ln(2\lambda_{\rm t}/b) + 1/2]$ are the resistive coefficients.

The following equations describe the resistive force and resistive torque exerted by the load sphere:

$$\begin{aligned} F_{\rm p} &= 6\pi\mu r\dot{X}, \\ T_{\rm p} &= 8\pi\mu r^3\dot{\theta}. \end{aligned} \tag{4}$$

By substituting Eqs. (2)–(4) into Eq. (1), the microrobot system is mathematically modeled as follows:

$$\begin{aligned} \dot{X} &= V, \\ \dot{V} &= -\frac{U_0\pi}{mL}\left[2\cos\left(\frac{2\pi X}{L}\right) + \cos\left(\frac{4\pi X}{L}\right)\right] \\ &\quad + \mathcal{A}V + \mathcal{B}\omega + \xi_1(t), \\ \dot{\theta} &= \omega, \\ \dot{\omega} &= \mathcal{C}V + \mathcal{D}\omega + \xi_2(t), \end{aligned} \tag{5}$$

where $\mathcal{A} = -[L_{\rm t}(C_{\rm tt}\cos^2\beta + C_{\rm tn}\sin^2\beta)\sec\beta + 6\pi\mu r]/m$, $\mathcal{B} = L_{\rm t}(C_{\rm tt} - C_{\rm tn})A_{\rm t}\sin\beta/m$, $\mathcal{C} = L_{\rm t}(C_{\rm tt} - C_{\rm tn})A_{\rm t}\sin\beta/J$, $\mathcal{D} = [L_{\rm t}(C_{\rm tt}\sin^2\beta + C_{\rm tn}\cos^2\beta)A_{\rm t}^2\sec\beta + 4\pi\mu b^2 L_{\rm t}\cos\beta - 8\pi\mu r^3]/J$, V denotes the velocity and ω represents the angular velocity.

In summary, the resulting system (5) captures the microrobot's coupled translational and rotational dynamics under both deterministic forces and stochastic disturbances. The explicit inclusion of GCN and GWN accounts for realistic environmental fluctuations, enabling more accurate modeling of microrobot behavior in complex microfluidic settings. This framework serves as the theoretical basis for analyzing propulsion performance, noise-induced transport phenomena and trajectory stability in the following sections.

3. Results and discussion

In this section, the effects of various parameters on the microrobot's dynamic response, average velocity, MFPT and propulsion efficiency are investigated. The simulations are carried out using a stochastic Runge–Kutta method (order 4) in MATLAB. Table 1 summarizes the geometric characteristics of the microrobot.

Table 1. Geometrical parameters.

Parameters	Values
r	8×10^{-3} m
$L_{\rm t}$	8×10^{-3} m
$A_{\rm t}$	4×10^{-3} m
$\lambda_{\rm t}$	2×10^{-3} m
b	2×10^{-5} m
$\rho_{\rm p}$	6500 kg·m^{-3}
$\rho_{\rm t}$	2500 kg·m^{-3}

3.1. Steady-state response at $\tau_1 \to 0$

When $\tau_1 \to 0$, GCN degenerates into GWN, and the probability density function (PDF) of the system (5) satisfies the Fokker–Planck–Kolmogorov equation

$$\begin{aligned} &\frac{\partial p(X,V,\theta,\omega)}{\partial t} \\ &= -\frac{\partial}{\partial X}(Vp) - \frac{\partial}{\partial V}\left(\left\{-\frac{U_0\pi}{mL}\left[2\cos\left(\frac{2\pi X}{L}\right)\right.\right.\right. \\ &\quad \left.\left.\left. + \cos\left(\frac{4\pi X}{L}\right)\right] + \mathcal{A}V + \mathcal{B}\omega\right\}p\right) \\ &\quad - \frac{\partial}{\partial\theta}(\omega p) - \frac{\partial}{\partial\omega}\left[(\mathcal{C}V + \mathcal{D}\omega)p\right] \\ &\quad + D_1\frac{\partial^2 p}{\partial V^2} + D_2\frac{\partial^2 p}{\partial\omega^2}, \end{aligned} \tag{6}$$

which adheres to the periodic boundary condition and the initial condition. When the system has reached a stable state in one period, that is $\partial p/\partial t = 0$ on the basis of the isotropic diffusion,[53,54] Eq. (6) satisfies the equilibrium condition $\mathcal{C}D_1/\mathcal{A} = \mathcal{B}D_2/\mathcal{D}$. It has a stationary solution for the PDF in the following form:

$$\begin{aligned} &p(X,V,\theta,\omega) \\ &= C\exp\left(\frac{\mathcal{A}}{D_1}\left\{\frac{1}{2}V^2 + \frac{U_0}{m}\left[\sin\left(\frac{2\pi X}{L}\right)\right.\right.\right. \\ &\quad \left.\left.\left. + 0.25\sin\left(\frac{4\pi X}{L}\right)\right]\right\} + \frac{\mathcal{D}}{2D_2}\omega^2\right), \end{aligned} \tag{7}$$

where C is the normalization constant.

The results are verified by comparing with the theoretical solution of the PDF of the response of the system. In Fig. 2, the model assumes GWN with $D_1 = \mathcal{A}\mathcal{B}D_2/(\mathcal{C}\mathcal{D})$, where $D_2 = 0.5$ J·(Pa·s)$^{-1}$, 0.7 J·(Pa·s)$^{-1}$, 0.9 J·(Pa·s)$^{-1}$. It can be observed that as the noise intensity gradually increases, the fluctuations of the microrobot's velocity and angular velocity in the time domain become significantly larger, and

the microrobot system exhibits more pronounced stochastic responses. This phenomenon indicates that stronger random disturbances can substantially reduce the stability of the microrobot's motion and increase the unpredictability of its trajectory. On the contrary, as the fluid viscosity increases, where $\mu = 0.003$ Pa·s, 0.005 Pa·s, 0.007 Pa·s, the fluctuation ranges of velocity and angular velocity gradually decrease in Fig. 3. This behavior is closely related to the damping effect of the fluid environment on the microrobot's motion. A higher-viscosity fluid can effectively suppress the microrobot's movement: the viscous resistance experienced by the microrobot is larger, its response is slower and its sensitivity to external noise is reduced, manifesting as enhanced convergence in its dynamical response. It is noteworthy that under various combinations of noise intensity and fluid viscosity, the theoretical analytical solutions remain in excellent agreement with the numerical simulation results. This not only validates the correctness of the theoretical model but also demonstrates the reliability and applicability of the established microrobot motion model under the combined effects of stochastic disturbances and viscous resistance.

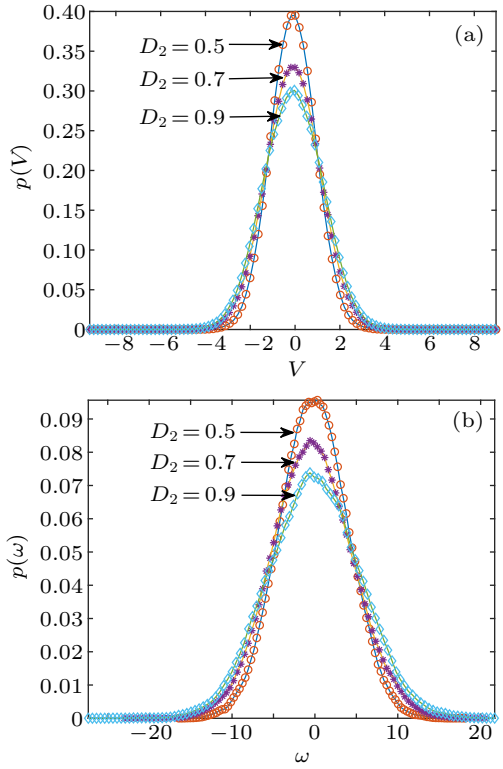


Fig. 2. The steady-state PDF of a microrobot system under different noise intensities when $\tau_1 \to 0$. (−) Theoretical results, (∘ ∗ ⋄) numerical results. (a) Marginal PDF of movement speed. (b) Marginal PDF of angular velocity. $\mu = 0.001$ Pa·s, $U_0 = 0.5$ J, $L = 1$ m.

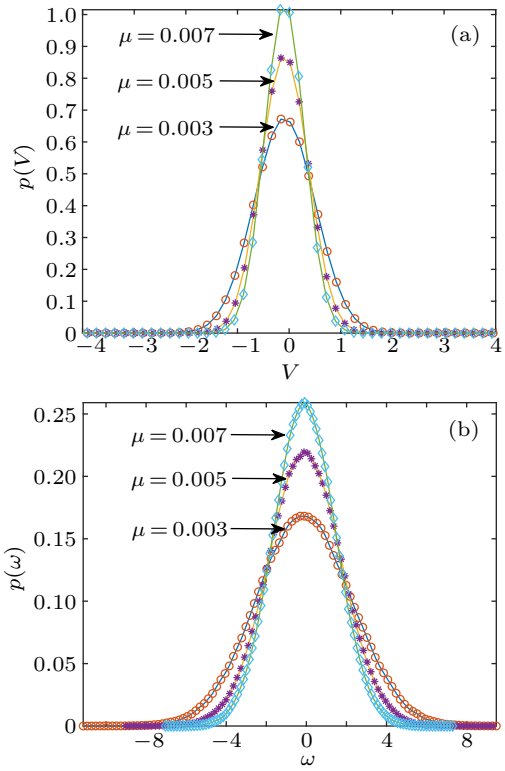


Fig. 3. The steady-state PDF of a microrobot system under different fluid viscosities when $\tau_1 \to 0$. (−) Theoretical results, (∘ ∗ ⋄) numerical results. (a) Marginal PDF of movement speed. (b) Marginal PDF of angular velocity. $D_2 = 0.5$ J·(Pa·s)$^{-1}$, $U_0 = 0.5$ J, $L = 1$ m.

3.2. Influence of ratchet potential on system speed

When $\tau_1 \neq 0$, $\xi_1(t)$ is GCN, which can be generated by the Ornstein–Uhlenbeck equation $\dot{\xi}_1(t) + \xi_1(t)/\tau_1 = \eta(t)$, where $\eta(t)$ denotes a zero mean GWN with the correlation function $\langle \eta(t)\eta(t_0)\rangle = 2D_1/\tau_1^2 \delta(t - t_0)$. In this case, its PDF satisfies the FPK equation

$$\begin{aligned}
&\frac{\partial p(X,V,\theta,\omega,\xi_1)}{\partial t} \\
&= -\frac{\partial}{\partial X}(Vp) - \frac{\partial}{\partial V}\left(\left\{-\frac{U_0\pi}{mL}\left[2\cos\left(\frac{2\pi X}{L}\right)\right.\right.\right. \\
&\quad \left.\left.\left. + \cos\left(\frac{4\pi X}{L}\right)\right] + \mathcal{A}V + \mathcal{B}\omega\right\}p\right) \\
&\quad - \frac{\partial}{\partial \theta}(\omega p) - \frac{\partial}{\partial \omega}\left[(\mathcal{C}V + \mathcal{D}\omega)p\right] \\
&\quad - \frac{\partial}{\partial V}(\xi_1 p) + \frac{\partial}{\partial \xi_1}\left(\frac{\xi_1 p}{\tau_1}\right) + \frac{D_1}{\tau_1^2}\frac{\partial^2 p}{\partial \xi_1^2} + D_2\frac{\partial^2 p}{\partial \omega^2}. \qquad (8)
\end{aligned}$$

Finding the exact solution of Eq. (8) is a challenging task; even finding the steady-state solution is quite complicated. When a microrobot is affected by GCN, i.e., $\tau_1 \neq 0$, analyzing the motion characteristics of the microrobot using the theoretical solution of the system is difficult. In this context, the impact of the related system parameters on the average velocity of the microrobot will be studied numerically.

Analyzing the effect of ratchet potential parameters on the average velocity of a microrobot enables a comprehensive understanding of its dynamic behavior within a complex potential field. It can be seen from Fig. 4 that the average velocity of the system is negative, indicating that the microrobot moves in the negative direction. In Fig. 4(a), when the microrobot is affected by GWN, the average velocity gradually decreases in the negative direction with the increase of

the slope of the ratchet potential. Due to the lack of temporal correlation in GWN, the induced motion becomes effectively directionless in the potential field, which makes the driving effect of noise on the microrobot's movement more dispersed. Moreover, a steeper ratchet potential increases the energy barriers, making directional transport more difficult. In contrast, when the microrobot is affected by GCN, the average velocity of the microrobot increases gradually in the negative direction with the increase in the slope of the ratchet potential. GCN has time correlation, which helps the microrobot overcome potential barriers in the ratchet potential and pushes it to move in the negative direction. Figure 4(b) shows that regardless of whether the microrobot is affected by GWN or GCN, the average velocity of the microrobot gradually increases in the negative direction with the increase in the ratchet potential period. A longer ratchet potential period reduces the potential energy obstacles encountered by the microrobot in the movement process, making the noise more significant in promoting its movement. Furthermore, an increase in fluid viscosity results in greater motion resistance, which decreases the microrobot's speed in a complex potential field. As illustrated in Fig. 4(c), when the microrobot is subjected to GCN, its average velocity gradually increases in the negative direction as the slope of the ratchet potential becomes steeper. This trend is consistent with that observed in Fig. 4(a). Moreover, the microrobot's average velocity increases in the negative direction with increasing correlation time τ_1, indicating that tuning τ_1 can enhance its directional motion. Figure 4(d) shows that with increasing ratchet potential period, the average velocity in the negative direction continues to rise. In this case as well, a longer correlation time τ_1 further amplifies the negative velocity, suggesting that the combined effect of an extended potential period and temporal correlation enhances the ability of GCN to drive the microrobot more effectively through the ratchet potential.

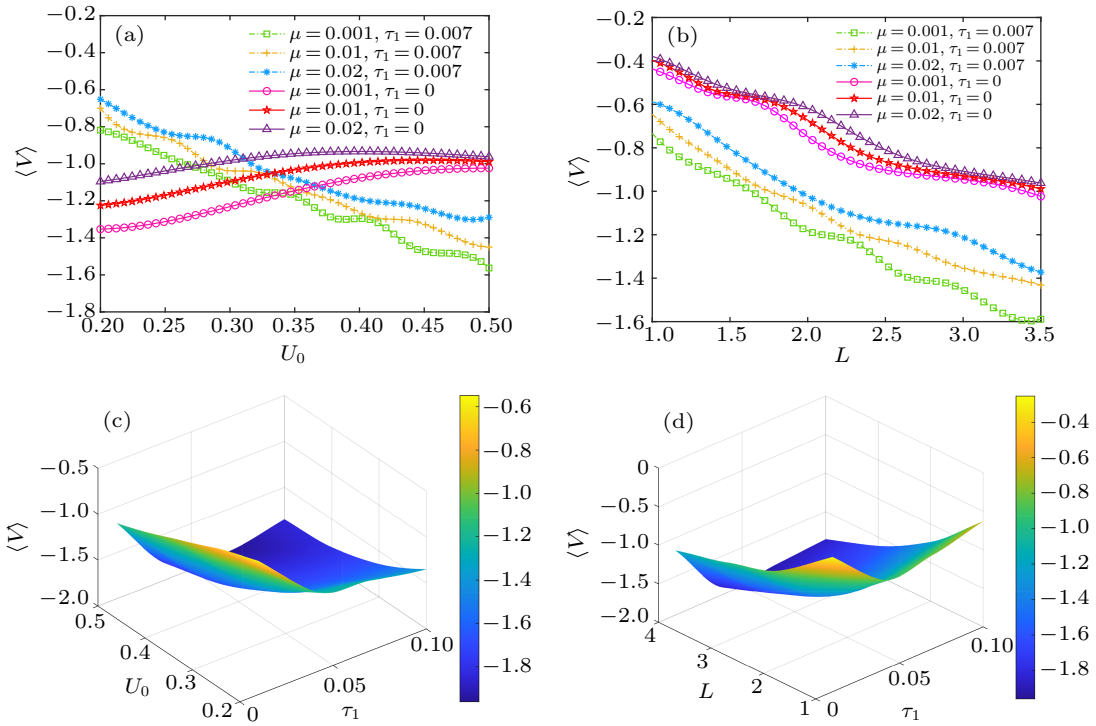


Fig. 4. Changes in the average velocity of the microrobot under the influence of ratchet potential parameters: (a) variation of U_0 at $L = 3.5$ m; (b) variation of L at $U_0 = 0.5$ J; (c) variation of U_0 and τ_1 at $L = 3.5$ m, $\mu = 0.004$ Pa·s; (d) variation of L and τ_1 at $U_0 = 0.5$ J, $\mu = 0.004$ Pa·s. $D_1 = 0.0003$ J·(Pa·s)$^{-1}$, $D_2 = 0.0002$ J·(Pa·s)$^{-1}$.

3.3. Influence of noise intensity on system speed

A detailed investigation of the influence of noise intensity on the average velocity of the microrobot can provide important insights into the mechanisms by which stochastic disturbances affect its motion. As shown in Figs. 5(a) and 5(b), when the noise intensity $D_2 = 0.0002$ J·(Pa·s)$^{-1}$ and D_1 gradually increases, the microrobot's average velocity in the negative direction decreases progressively. This phenomenon can be attributed to the increase in D_1, which subjects the microrobot to stronger random forces within the potential field, thereby reducing its motion stability in the complex landscape. Such disturbances weaken the microrobot's ability to move directionally along the negative direction, resulting in a gradual decrease in its average velocity. In Figs. 5(c) and 5(d), when $D_1 = 0.0001$ J·(Pa·s)$^{-1}$ and D_2 gradually increases, the microrobot's average velocity remains nearly unchanged. D_2 primarily affects the rotational degrees of freedom of the microrobot, influencing fluctuations in angular velocity and randomness in rotational direction, but has a relatively weak direct effect on linear motion. In a periodic potential field, the direc-

tional transport of the microrobot is mainly driven by forces along the forward direction rather than solely controlled by rotational behavior. Although the rotational motion exhibits stronger randomness as D_2 increases, such disturbances do not significantly alter the microrobot's average velocity along the periodic potential. Under these conditions, the microrobot's average velocity remains relatively stable. These results indicate that the influence of noise intensity on the microrobot's motion behavior exhibits significant differences. An increase in D_1 substantially reduces the microrobot's ability for directional motion, whereas changes in D_2 have little effect on its average velocity. This finding provides a new perspective for understanding the role of noise in microrobot dynamics and offers a modeling basis for optimizing its motion control strategies.

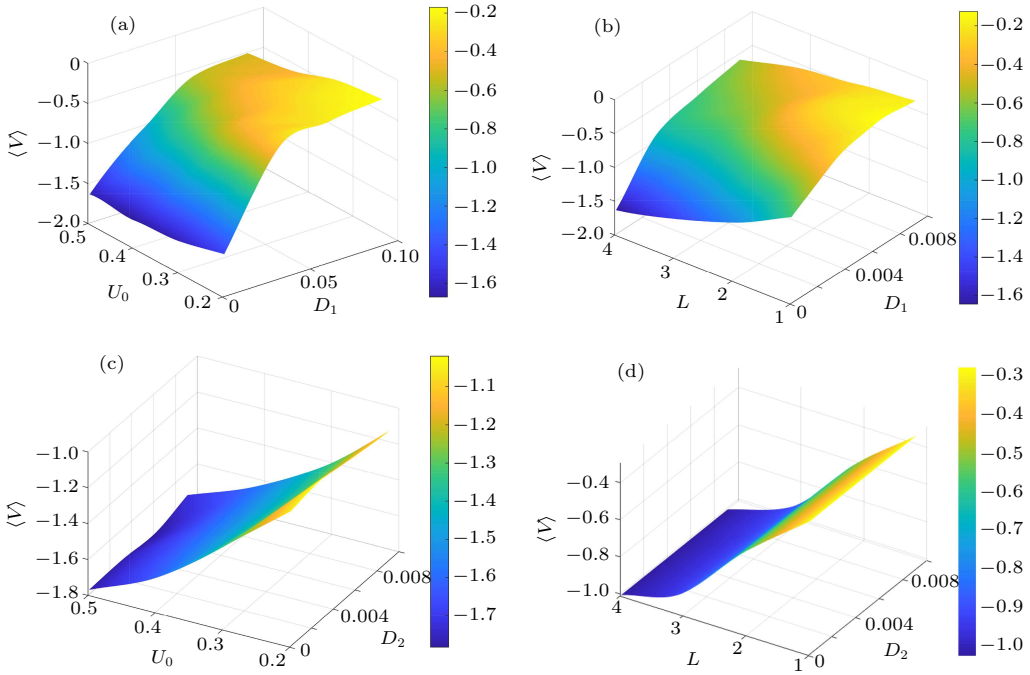


Fig. 5. Changes in the average velocity of the microrobot under the influence of noise intensity: (a) variation of U_0 and D_1 at $D_2 = 0.0002$ J·(Pa·s)$^{-1}$, $L = 4$ m; (b) variation of L and D_1 at $D_2 = 0.0002$ J·(Pa·s)$^{-1}$, $U_0 = 0.5$ J; (c) variation of U_0 and D_2 at $D_1 = 0.0001$ J·(Pa·s)$^{-1}$, $L = 4$ m; (d) variation of L and D_2 at $D_1 = 0.0001$ J·(Pa·s)$^{-1}$, $U_0 = 0.5$ J. $\mu = 0.004$ Pa·s, $\tau_1 = 0.01$ s.

3.4. Influence of ratchet potential and noise intensity on the MFPT

Investigating the impact of ratchet potential parameters and noise intensity on the MFPT provides a deeper understanding of the microrobot's motion mechanism within an asymmetric potential field while also indirectly indicating the transition rate of the microrobot system. According to formula (2), we need to calculate the two stable points

$$\begin{aligned} x_{s1} &= -L[\arccos(\sqrt{3}/2 - 1/2)]/2\pi, \\ x_{s2} &= -L[\arccos(\sqrt{3}/2 - 1/2)]/2\pi + L \end{aligned}$$

of the microrobot system within the interval $[-1, 1]$. The MFPT is defined as

$$\mathrm{MFPT}(x_{s1} \to x_{s2}) = \langle \inf\{t : x(t) > x_{s2} | x(0) = x_{s1}\} \rangle .$$

In order to ensure the accuracy of the calculation results, all the calculated values are higher than the average of the 200000 paths. Figure 6(a) shows that the MFPT of the microrobot system gradually increases with the slope of the ratchet potential U_0. This phenomenon indicates that a steeper potential slope corresponds to higher energy barriers, requiring more time for the microrobot to cross the barriers under stochastic disturbances, thus further constraining its dynamical transition process. A larger U_0 effectively increases the barrier that the microrobot must overcome to transition between potential wells, thereby slowing the rate at which it moves from one stable state to another. In addition, the figure shows that an increase in the correlation time τ_1 also significantly prolongs the MFPT. Since the ratchet potential itself has directional bias, it tends to drive the microrobot along the negative direction. The increase in τ_1 partially weakens the promoting effect of noise on motion in this direction, making it more difficult for the microrobot to complete effective transitions quickly, thus further increasing the MFPT. Figure 6(b) shows that the MFPT of the microrobot system gradually decreases as the noise intensity D_1 increases. An increase in D_1 corresponds to stronger random forces acting on the microrobot along the translational direction, which enhances the amplitude of trajectory fluctuations. Since the potential barriers of the ratchet potential represent the main obstacle for the microrobot along its principal motion direction, stronger stochastic disturbances increase dynamic pertur-

bations in the trajectory, making it easier to overcome the barriers and achieve transitions from one stable point to another. Therefore, the increase in D_1 effectively facilitates the transition process of the microrobot system, shortening the MFPT. Figure 6(c) further demonstrates that increasing the noise intensity D_2 does not significantly affect the MFPT of the microrobot system. This result indicates that the primary driving force for crossing the barriers of the ratchet potential is still the microrobot's translational motion, rather than its rotational behavior. Although D_2 induces perturbations in the rotational direction, these changes have limited impact on the directional transition behavior of the microrobot in the periodic potential and therefore exert only a weak influence on the MFPT.

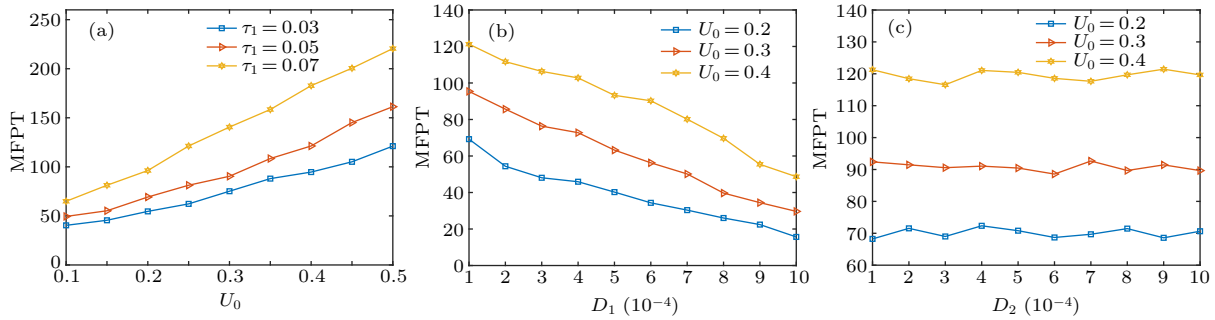


Fig. 6. The MFPT under the influence of the ratchet potential parameter and noise intensity: (a) variation of U_0 at $D_1 = 0.0007$ J·(Pa·s)$^{-1}$, $D_2 = 0.0002$ J·(Pa·s)$^{-1}$; (b) variation of D_1 at $\tau_1 = 0.05$ s, $D_2 = 0.0002$ J·(Pa·s)$^{-1}$; (c) variation of D_2 at $\tau_1 = 0.05$ s, $D_1 = 0.0007$ J·(Pa·s)$^{-1}$. $\mu = 0.004$ Pa·s, $L = 1$ m.

3.5. Influence of geometric parameters on efficiency

Analyzing the performance of various wavelengths and tail radii in a stochastic environment provides a comprehensive understanding of how the geometric parameters of a microrobot influence its propulsion efficiency. These insights can be used to optimize the microrobot's design in order to maintain efficient propulsion in random environments. The propulsion efficiency of a spiral microrobot is defined as $\langle\eta\rangle = \langle F_t\rangle\langle V\rangle / (\langle T_t\rangle\langle\omega\rangle)$,[55] where $\langle\cdot\rangle$ refers to the average over 10000 paths. As shown in Fig. 7(a), the propulsion efficiency of the microrobot exhibits a clear downward trend as the wavelength of the helical tail gradually increases. This phenomenon can be attributed to the fact that a longer wavelength leads to a larger pitch per unit length of the helical structure, thereby increasing the time required to complete one full helical cycle. When the period becomes longer, the effective propulsion distance generated per unit time decreases, resulting in an overall reduction in the microrobot's propulsion efficiency. Figure 7(b) shows that the propulsion efficiency gradually increases with the tail radius. An increase in the tail radius enhances the hydrodynamic effect of the helical tail, generating a larger propulsive force per unit rotation. Specifically, a larger tail radius provides a greater contact area, which improves the relative flow interaction between the helical tail and the surrounding fluid. This change enhances the stability and continuity of the helical propulsive force, thereby improving the propulsion efficiency. It is worth noting that Fig. 7 further reveals the effect of noise type on the propulsion performance of the microrobot. When GCN is introduced into the microrobot system, its propulsion efficiency is generally higher than that under GWN. This improvement arises from the temporal correlation of GCN, which generates a more continuous disturbance pattern, thereby promoting the stability and effectiveness of the microrobot's power output. In contrast, GWN has zero correlation time and produces completely random disturbances, which reduce the propulsion efficiency of the microrobot system. These findings provide new insights into optimizing microrobot propulsion performance in stochastic environments and offer valuable references for future research in this field.

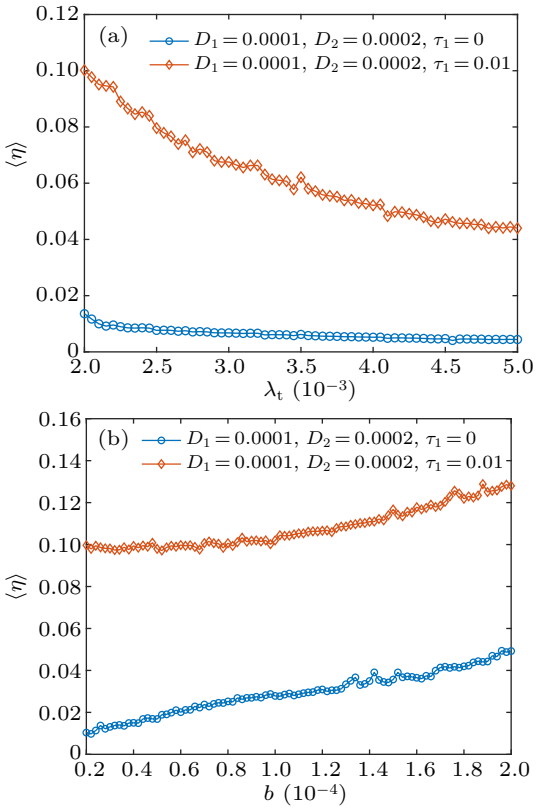


Fig. 7. The relationship between geometric parameters of the microrobot and the propulsion efficiency: (a) the propulsion efficiency under the influence of λ_t; (b) the propulsion efficiency under the influence of b. $\mu = 0.001$ Pa·s, $U_0 = 0.1$ J, $L = 1$ m.

4. Conclusions

This study presents a robust theoretical framework for analyzing the directional transport of a spiral microrobot navigating a ratchet potential under GCN excitation. Our findings reveal that the temporal correlations inherent in GCN significantly enhance the microrobot's ability to surmount potential barriers, thereby improving directional transport efficiency. Specifically, increasing the ratchet potential period or reducing fluid viscosity markedly boosts the microrobot's average velocity, while a lower potential slope combined with higher GCN intensity reduces the MFPT, enabling faster barrier transitions. Comparative analysis underscores that GCN outperforms GWN in enhancing propulsion efficiency, emphasizing the critical role of noise correlation in accurate microrobot modeling. These insights deepen the theoretical understanding of stochastic dynamics in microrobotic systems and offer practical strategies for optimizing their design and performance in complex microfluidic environments. Future work could explore experimental validation of these findings and extend the model to account for multi-dimensional noise effects, further advancing microrobot applications in precision medicine and beyond.

Acknowledgements

The authors gratefully acknowledge fruitful discussions with Professor Yong Xu and Associate Professor Yongge Li K. Suleiman thanks the support of the National Natural Science Foundation of China (Grant No. W2533021).

References

[1] Lee J G, Raj R R, Day N B and Shields IV C W 2023 *ACS Nano* **17** 14196
[2] Liang C, Zhan C, Zeng F, Xu D, Wang Y, Zhao W, Zhang J, Guo J, Feng H and Ma X 2018 *ACS Applied Materials & Interfaces* **10** 35099
[3] Xie J, Bi C, Cappelleri D J and Chakraborty N 2021 *Journal of Mechanisms and Robotics* **13** 041005
[4] Kim D i, Lee H, Kwon S h, Choi H and Park S 2019 *Sensors and Actuators B: Chemical* **289** 65
[5] Vyskocil J, Mayorga-Martinez C C, Jablonská E, Novotny F, Ruml T and Pumera M 2020 *ACS Nano* **14** 8247
[6] Li S, Ying Y, Jiang T and Nie D 2024 *Chin. Phys. B* **33** 124701
[7] Demircali A A, Varol R, Erkan K and Uvet H 2021 *Journal of Mechanisms and Robotics* **13** 061005
[8] Ahmed D, Sukhov A, Hauri D, Rodrigue D, Maranta G, Harting J and Nelson B J 2021 *Nature Machine Intelligence* **3** 116
[9] Lu K, Zhou C, Li Z, Liu Y, Wang F, Xuan L and Wang X 2024 *Lab on a Chip* **24** 446
[10] Zöttl A and Stark H 2023 *Annual Review of Condensed Matter Physics* **14** 109
[11] Lou X, Yu N, Chen K, Zhou X, Podgornik R and Yang M 2021 *Chin. Phys. B* **30** 114702
[12] Wang W, He Y, Liu H, Guo Q, Ge Z and Yang W 2023 *Sensors and Actuators A: Physical* **360** 114567
[13] Alapan Y, Yasa O, Yigit B, Yasa I C, Erkoc P and Sitti M 2019 *Annual Review of Control, Robotics, and Autonomous Systems* **2** 205
[14] Zhang F, Zhuang J, Li Z, Gong H, de Ávila B E F, Duan Y, Zhang Q, Zhou J, Yin L, Karshalev E, *et al*. 2022 *Nat. Mater.* **21** 1324
[15] Ussia M and Pumera M 2022 *Chemical Society Reviews* **51** 1558
[16] Li H, Tan J and Zhang M 2008 *IEEE Transactions on Automation Science and Engineering* **6** 220
[17] Zhou H, Mayorga-Martinez C C, Pané S, Zhang L and Pumera M 2021 *Chemical Reviews* **121** 4999
[18] Zhang Z, Wang Y, Kang J, Qiu X and Wang C 2022 *Soft Matter* **18** 6148
[19] Xu T, Yu J, Vong C I, Wang B, Wu X and Zhang L 2019 *IEEEASME Transactions on Mechatronics* **24** 924
[20] Caldag H O and Yesilyurt S 2019 *Journal of Fluids and Structures* **90** 164
[21] Rein C, Kolář M, Kroy K and Holubec V 2023 *Europhys. Lett.* **142** 31001
[22] Reichhardt C O and Reichhardt C 2017 *Annual Review of Condensed Matter Physics* **8** 51
[23] Paneru G, Park J T and Pak H K 2021 *The Journal of Physical Chemistry Letters* **12** 11078
[24] Patil G, Mandal P and Ghosh A 2022 *Phys. Rev. Lett.* **129** 198002
[25] Berdakin I, Silhanek A V, Moyano Cortéz H N, Marconi V I and Condat C A 2013 *Central European Journal of Physics* **11** 1653
[26] Wen Y, Li Z, Wang H, Zheng J, Tang J, Xu X, Lai P Y and Tong P 2025 *The Journal of Chemical Physics* **162** 204903
[27] Roberts C and Zhen Z 2023 *Phys. Rev. E* **108** 014139
[28] Nabil M, Frankowski A, Orosa A, Fuller A and Nourhani A 2022 *Phys. Rev. E* **105** 054610
[29] Ai B Q and Li F G 2017 *Soft Matter* **13** 2536
[30] Kulić I, Thaokar R and Schiessel H 2005 *Europhys. Lett.* **72** 527
[31] Lozano C, Liebchen B, Ten Hagen B, Bechinger C and Löwen H 2019 *Soft Matter* **15** 5185
[32] Ramos-Docampo M A, Fernández-Medina M, Taipaleenmaki E, Hovorka O, Salgueiriño V and Stadler B 2019 *Acs Nano* **13** 12192
[33] Ai B Q and Wu J C 2014 *The Journal of Chemical Physics* **140** 094103
[34] Ghosh A, Paria D, Singh H J, Venugopalan P L and Ghosh A 2012 *Phys. Rev. E* **86** 031401
[35] Jahanshahi S, Löwen H and Ten Hagen B 2017 *Phys. Rev. E* **95** 022606
[36] Ghosh A, Paria D, Rangarajan G and Ghosh A 2014 *The Journal of Physical Chemistry Letters* **5** 62
[37] Ryan P and Diller E 2017 *IEEE Transactions on Robotics* **33** 1398
[38] Xu Y , Mei R , Li Y and Kurths J 2019 *Stochastic Dynamics Out of Equilibrium* **282** 443
[39] Ye S, Liu P, Ye F, Chen K and Yang M 2020 *Soft Matter* **16** 4655
[40] Smyk S, Telezki V, Riepl J, Hayes J and Klumpp S 2021 *Euro. Phys. J. Spec. Top.* **230** 1099
[41] Huang C, Ding M and Xing X 2020 *Phys. Rev. Research* **2** 043222
[42] Wang B, Wu Y, Zhang X and Chen H 2021 *Physica A* **565** 125543
[43] Fiasconaro A and Spagnolo B 2009 *Phys. Rev. E* **80** 041110
[44] Wang B and Wu W 2024 *Mod. Phys. Lett. B* **38** 2350202
[45] Kazakevičius R and Ruseckas J 2015 *J. Stat. Mech.: Theor. Exper.* **2015** P02021
[46] Koumakis N, Maggi C and Di Leonardo R 2014 *Soft Matter* **10** 5695
[47] Ghosh P K, Misko V R, Marchesoni F and Nori F 2013 *Phys. Rev. Lett.* **110** 268301
[48] Xu Y, Liu X, Li Y and Metzler R 2020 *Phys. Rev. E* **102** 062106
[49] Zhang Y, Jin Y and Xu P 2020 *International Journal of Mechanical Sciences* **172** 105418
[50] Das S, Gompper G and Winkler R G 2018 *New J. Phys.* **20** 015001
[51] Patil G and Ghosh A 2023 *Euro. Phys. J. Spec. Top.* **232** 927
[52] San Ha N and Goo N S 2010 *Journal of Bionic Engineering* **7** 259
[53] Shi X, Li Y, Xu Y and Liu Q 2024 *Theoretical and Applied Mechanics Letters* **14** 100534
[54] Darling D and Siegert J 1957 *IRE Transactions on Information Theory* **3** 32
[55] Chattopadhyay S, Moldovan R, Yeung C and Wu X 2006 *Proc. Natl. Acad. Sci. USA* **103** 13712